

Doubly excited states of beryllium and magnesium

Patrick F. O'Mahony

Department of Physics, University of Chicago, Chicago, Illinois 60637

Chris H. Greene

Department of Physics and Astronomy, Louisiana State University, Baton Rouge, Louisiana 70803

(Received 15 May 1984)

The noniterative eigenchannel R -matrix method is used to study the properties of the valence electrons in Be and Mg $^1P^o$ states. Our results detail the evolution of electron correlations as a function of energy. Besides obtaining an improved quantitative description of doubly excited states in these atoms, we verify the conclusion of an earlier hyperspherical-coordinate study that the wave functions are exact analogs of the $sp +$ and $sp -$ states of helium and H^- .

I. INTRODUCTION

This paper continues the study of the correlated motion of two electrons which had recently been extended to the alkaline earths¹ [Ref. 1(a) is hereafter referred to as I]. The spectrum of doubly excited $^1P^o$ states of helium converging to the He^+ ($n=2$) threshold had been classified² as being approximately represented by superpositions of $2snp$ and $2pns$ with coefficients of equal amplitude, i.e., $2snp \pm 2pns$, the so-called plus or minus states. Later Macek³ showed that this classification emerged naturally from a study of the wave functions in hyperspherical coordinates. Greene then demonstrated in I that the $^1P^o$ states of Be with autoionizing resonances could also be described by wave functions that admix $1s^22sep$ and $1s^22pns$ with equal amplitude. That this equipartition may be a general rule in the alkaline earths was suggested by an analysis of the $^1P^o$ spectra of Ca, Sr, and Ba (Armstrong *et al.*⁴) showing that the lowest $^1P^o$ channels $nsn'p$ and $(n-1)dn'p$ for Ca ($n=4$), Sr ($n=5$), and Ba ($n=6$) mixed in nearly equal proportions. Theoretical verification of this equipartition rule in Be was the key result of the hyperspherical treatment given in I.

Reference 1 utilized hyperspherical coordinates as the natural coordinate system to examine the joint motion of two strongly interacting electrons outside a frozen core. Here instead we describe the motion of the two electrons in a more conventional manner as a superposition of numerical independent-particle wave functions of the two electrons. We emphasize the complementarity of the two approaches in studying the dynamics of the joint motion of the two electrons, noting that each may have its specific advantages depending on the process under study and on the specific aim of each study. We can interpret the behavior of the electron pair at different excitation energies by plotting its charge density as a function of the coordinates r_1 and r_2 (see Sec. III).

Calculationally we solve the Schrödinger equation of the two-electron system outside a frozen core in a volume V using a recently adapted version of the eigenchannel R -matrix⁵ approach. Outside V we join these solutions to Coulomb functions, hence obtaining a reaction matrix.

Diagonalization of this reaction matrix gives the multichannel quantum-defect (MQDT) parameters⁶ and the eigenmodes. Interpretation of these parameters as a function of energy gives valuable insight into the underlying dynamics of the system, as well as providing energy levels, oscillator strengths, etc.

Our results show better quantitative agreement with experiment and with recent calculations for Be than I; its basic conclusions, however, are confirmed. We also show explicitly that the Mg autoionizing resonances similarly obey the equipartition rule and we calculate the photoionization cross sections, energy levels, etc. for both Be and Mg, obtaining good agreement with experiment and with previous calculations. Although our calculations show good quantitative agreement with experiment, our main aim is to study the dynamics of the two-electron system by analyzing the wave functions as a function of the excitation energy of the system.

Section II describes the calculational procedure. Section III presents the results obtained for Be and Mg. Section IV gives a discussion and a summary of the results.

II. CALCULATIONAL PROCEDURE

A. General formulation

A noniterative reformulation of the eigenchannel R -matrix method⁷ was presented recently.⁵ It enables one to variationally calculate the R matrix, and from it the quantum defects and other parameters of the eigenchannels at any given energy E , by a single diagonalization. The main results of Ref. 5 to be used here are outlined below.

We write the total energy E as

$$E = \frac{\int_V \psi H \psi dV}{\int_V \psi \psi dV} = \frac{\int_V \psi (-\frac{1}{2}\nabla^2 + U) \psi dV}{\int_V \psi \psi dV} \quad (1)$$

using atomic units, real wave functions, and

$$\vec{\nabla} = \sum_i \vec{\nabla}_i, \quad U = -\sum_i \frac{Z}{r_i} + \sum_i \sum_{j(<i)} \frac{1}{r_{ij}}. \quad (2)$$

Letting

$$\psi = \sum_k c_k y_k \quad (3)$$

and taking $\partial E / \partial c_k = 0$ would give the usual minimum principle for E . Instead we wish to obtain a variational expression for the normal logarithmic derivative b defined by

$$\frac{\partial \psi}{\partial n} + b\psi = 0 \quad (4)$$

on the surface S of the reaction volume V . Integrating (1) by parts and substituting $\partial \psi / \partial n$ from (4) we get

$$b = \frac{\int_V [-(\vec{\nabla} \psi) \cdot (\vec{\nabla} \psi) + 2\psi(E - U)\psi] dV}{\int_S \psi \psi dS} \quad (5)$$

Substituting further, (3) into (5), gives

$$b = \frac{\sum_{k,l} c_k \Gamma_{kl} c_l}{\sum_{k',l'} c_{k'} \Lambda_{k'l'} c_{l'}} \quad (6)$$

where

$$\Gamma_{kl} = \int_V [-(\vec{\nabla} y_k) \cdot (\vec{\nabla} y_l) + 2y_k(E - U)y_l] dV, \quad (7)$$

and

$$\Lambda_{kl} = \int_S y_k y_l dS. \quad (8)$$

Taking $\partial b / \partial c_k = 0$ yields the generalized eigenvalue problem

$$\underline{\Gamma} \vec{c} = b \underline{\Lambda} \vec{c}, \quad (9)$$

with eigenvalues b_β and eigenvectors

$$\psi_\beta = \sum_k c_k^{(\beta)} y_k, \quad (10)$$

for a preselected value of the total energy E . These results provide the initial conditions for the wave function of an electron escaping into a Coulomb field outside the volume V . Interpretation and analysis of the eigenvectors (10) should aim at understanding the joint motion of the two electrons.

B. Two electrons outside a closed-shell core

The Hamiltonian for two interacting electrons outside a frozen core can be written approximately in a.u. as

$$H = -\frac{1}{2} \nabla_1^2 - \frac{1}{2} \nabla_2^2 + U(r_1) + U(r_2) + \frac{1}{r_{12}}, \quad (11)$$

where the Hartree-Slater core potential $U(r_i)$ replaces the Coulomb potential $-Z/r_i$ and part of $\sum_i \sum_{j(<i)} r_{ij}^{-1}$ in Eq. (2). For more quantitative purposes other potentials are probably preferable to the Hartree-Slater version, as discussed by Laughlin and Victor⁸ and by Lin.⁹

We focus on the Be channels $1s^2 2s\epsilon p$, $1s^2 2pns$, and $1s^2 2pnd \ ^1P^o$ in the energy range below the Be^+ ($2p$) threshold. The analogous channels in Mg are $1s^2 2s^2 2p^6 3s\epsilon p$, $1s^2 2s^2 2p^6 3pns$, and $1s^2 2s^2 2p^6 3pnd \ ^1P^o$, but we shall refer for brevity to Be alone.

With a frozen $1s^2$ core our task is to represent the wave

function of the two outer electrons by a superposition of independent-particle wave functions, adequate to describe the correlated motion within the volume V . Therefore for a pair of electrons coupled to a given $\vec{L} = \vec{L}_1 + \vec{L}_2$ within V we write

$$\psi = A \sum_{n,m} c_{nm} \phi_{n l_1}(r_1) F_{m l_2}(r_2) Y_{l_1 l_2 L M_L}(\theta_1 \phi_1, \theta_2 \phi_2), \quad (12)$$

where A denotes antisymmetrization. The following set of energy-independent orbitals were used: the $2snp$ configurations were represented by products of the Hartree-Slater orbital of Be^+ $\phi_{2s}(r_1)$ and of the following ten np orbitals $F_{np}(r_2)$. Five of these orbitals were obtained by numerically solving the one-electron radial Schrödinger equation using the Hartree-Slater potential¹⁰ of an $l=1$ electron in the field of a Be^+ ion subject to the condition that each orbital vanish on the boundary $r=r_0=9$ a.u. which encloses the charge distributions of $\text{Be}^+(2s)$ and $\text{Be}^+(2p)$. [Note that this potential, used to define the variational orbitals, differs from the potential U in Eq. (11).] The other five np orbitals were found by integration in the same potential at five different energies which yield nonzero values of the orbitals on the boundary and a variety of logarithmic derivatives. The energies of these orbitals are given in Table I as an illustration. Note that these np wave functions are not in general orthogonal to one another but they are orthogonal to the $1s$ core orbitals. Taking a nonorthogonal basis set provides added flexibility at the cost of including overlap integrals in the matrices $\underline{\Gamma}$ and $\underline{\Lambda}$. Similarly, nine functions were taken for the ns in the $2pns$ channel and ten for the nd in the $2pnd$ channel. Convergence tests showed that the influence of higher "strongly closed" channels, such as $3pns$ in Be or $4pns$ in Mg, is negligible in the energy range below the first excited threshold of each ion.

Substitution of these 29 wave functions into (7) and (8) and subsequent evaluation of the matrix elements leads to the generalized eigenvalue problem (9). For the solution of this problem the rank of the $\underline{\Lambda}$ matrix is essential. In our case the $\underline{\Lambda}$ matrix reduces to 3 diagonal blocks of nonzero elements, one for each of the $2s\epsilon p$, $2pns$, and $2pnd$ channels. Each of these block matrices is of rank 1. Therefore 26 of the 29 equations of (9) may serve to eliminate as many of the unknown coefficients c , the other three equations giving three eigenvalues. Solving Eq. (9)

TABLE I. Orbital energies of the np states.

Orbital	Energy relative to $\text{Be}^+(2s)$ threshold (a.u.)
1	-0.167
2	0.023
3	0.321
4	0.756
5	1.317
6	-0.250
7	-0.072
8	0.173
9	0.540
10	1.037

with standard routines, we then get three eigenvalues b_β and three ψ_β in the form (12) with eigenvectors $c_{nm}^{(\beta)}$. Examination of these eigenvectors as functions of the total energy, to reveal the dynamics of the two-electron system, will be pursued in Sec. III.

Outside V the field is Coulombic and the escaping electron's wave function can be represented by a superposition of the energy-normalized regular and irregular Coulomb functions f and g .⁶

$$\langle \phi_i | \psi_\beta \rangle = f_i(\epsilon_i, r_0) I_{i\beta} - g_i(\epsilon_i, r_0) J_{i\beta}, \quad r \geq r_0 \quad (13a)$$

$$\begin{aligned} \left\langle \phi_i \left| \frac{\partial \psi_\beta}{\partial r} \right. \right\rangle &= -b_\beta \langle \phi_i | \psi_\beta \rangle \\ &= \frac{\partial}{\partial r} f_i(\epsilon_i, r) I_{i\beta} - \frac{\partial}{\partial r} g_i(\epsilon_i, r) J_{i\beta}, \\ & \quad r = r_0. \end{aligned} \quad (13b)$$

Here ϕ_i represents either the $\text{Be}^+(2s)$ or $\text{Be}^+(2p)$ ionic states, together with the spin and orbital couplings of the escaping electron,⁶ and $\epsilon_i = E - E_{\text{ion}}^i$ is the electron energy relative to the ionization threshold of the i th channel. The coefficients $I_{i\beta}$ and $J_{i\beta}$ form two 3×3 matrices to be determined by matching the solutions and their derivatives [Eq. (13)] at $r = r_0$ to those given by Eq. (12).

The reaction matrix \underline{K} is defined by

$$\underline{K} = \underline{J} \underline{I}^{-1}. \quad (14)$$

Diagonalizing it,

$$\underline{U}^T \underline{K} \underline{U} = \tan(\pi \underline{\mu}), \quad (15)$$

we obtain the eigenvalues $\tan(\pi \mu_\alpha)$ and the eigenvectors \underline{U} . The eigenchannels of the short-range reaction matrix are obtained from the ψ_β by the transformation

$$\psi_\alpha = \sum_{\beta, i} \psi_\beta (\underline{I}^{-1})_{\beta i} U_{i\alpha} \cos(\pi \mu_\alpha) \quad (16)$$

and have the usual asymptotic form

$$\begin{aligned} \psi_\alpha &= \sum_i \phi_i [f_i(\epsilon_i, r) U_{i\alpha} \cos(\pi \mu_\alpha) \\ & \quad - g_i(\epsilon_i, r) U_{i\alpha} \sin(\pi \mu_\alpha)], \quad r \geq r_0. \end{aligned} \quad (17)$$

The dipole velocity matrix elements associated with these eigenchannels are

$$D_\alpha = \omega^{-1} \int_V \psi_\alpha \left[\frac{\partial}{\partial z_1} + \frac{\partial}{\partial z_2} \right] \psi_0 dV, \quad (18)$$

where ψ_0 represents the ground-state wave function of Be and ω the photon energy in a.u. The energy levels and photoionization cross sections are determined by these quantities μ_α , $U_{i\alpha}$, and D_α . Explicit expressions can be found in Refs. 1 and 6.

III. RESULTS

A. Analysis of the beryllium wave functions

We focus initially on the two series $2s\epsilon p$ and $2pn s$, as their interaction with the $2pnd$ series is known to be weak.

We solve the 19×19 system of equations given by Eq. (9) for this two-channel case and proceed by matching the solutions to Coulomb functions on the boundary as described in Sec. II. The orthogonal matrix \underline{U} in this case is

$$\underline{U} = \begin{bmatrix} \cos\theta & \sin\theta \\ -\sin\theta & \cos\theta \end{bmatrix}, \quad (19)$$

a function of a single angle θ which measures the amount of mixing between the two channels $2s\epsilon p$ and $2pn s$. We diagonalize Eq. (9) at different energies in the region of interest, namely, from below the $1s^2 2s 2p$ bound state up to the $\text{Be}^+(2p)$ threshold. Proceeding as described in Sec. II we obtain the eigenvalues $\tan(\pi \mu_\alpha)$ and eigenvectors $U_{i\alpha}$ of the K matrix. Figure 1 shows the MQDT parameters θ/π and eigenquantum defects μ_1 and μ_2 in this range. Studying these parameters as functions of energy helps to unravel the dynamics of the electron pair.

The most striking feature in Fig. 1(a) is the rise of θ from no mixing ($\theta \sim 0$) at low energies to approximately equal mixing ($\theta \sim \pi/4$) at higher energies. This transition was first demonstrated in I, although we find some quantitative differences. In particular, the transition occurs somewhat more smoothly here, over an energy range $\Delta E \sim 0.2$ Ry as compared with $\Delta E \sim 0.1$ Ry in I. Also, our eigenquantum defects μ_1 and μ_2 in Fig. 1(b) do not show the rapid variations below the $2s$ threshold which

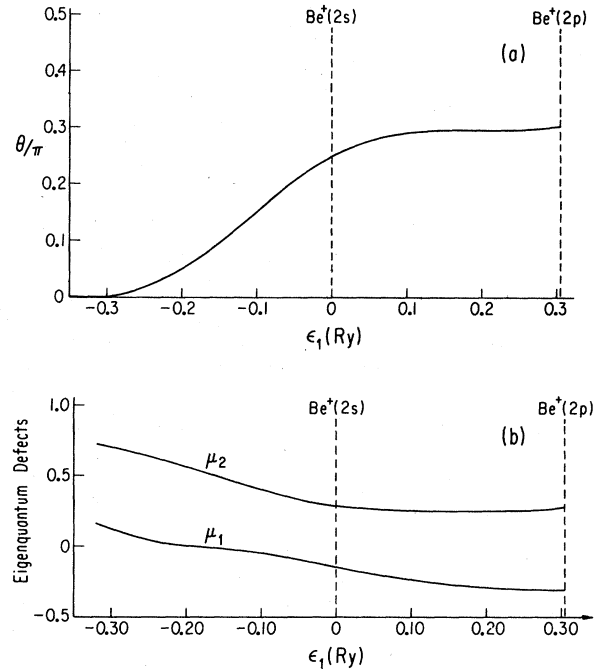


FIG. 1. Final-state quantum-defect parameters for beryllium as functions of the energy ϵ_1 relative to the $2s$ threshold. Shown are (a) mixing angle and (b) eigenquantum defects. [Note: A different phase convention was used in Fig. 5 of I, in which $\theta \rightarrow \pi/2$ at low energies in the region of zero mixing and therefore μ_1 was associated with channel 2 and μ_2 with channel 1. This should be kept in mind when comparing earlier results (Ref. 11) with our present calculation.]

were obtained in I. These differences seem to reflect numerical inaccuracies in the earlier study^{1(a)} which became most acute at negative energies. This is discussed further in Sec. IV below.

The change from zero to approximately equal mixing was explained in I in terms of the energy dependence of the two-electron wave function. Here we confirm and document this energy dependence more thoroughly by plotting the charge densities $|\Psi_\alpha(\vec{r}_1, \vec{r}_2)|^2$ at several energies. The shape of the potential energy of the two electrons is crucial to the argument, so we begin by examining this potential in helium.

The potential given by

$$U(r_1, r_2) = -\frac{2}{r_1} - \frac{2}{r_2} + \frac{1}{(r_1^2 + r_2^2 - 2r_1r_2\cos\theta_{12})^{1/2}} \quad (20)$$

is shown in Fig. 2 for a particular value of θ_{12} . The potential rises about the line $r_1 = r_2$ and has two valleys. One, at $r_1 \sim 0$ and $r_2 \gg r_1$, corresponds to one of the electrons being close to the ion and the other being in an excited bound or continuum state. The second valley is at $r_2 \sim 0$; $r_1 \gg r_2$. The potential is of course symmetric about the line $r_1 = r_2$. Two degrees of freedom in the (r_1, r_2) plane are singled out by the topology of this potential. In each valley there is a longitudinal coordinate which is represented asymptotically by the $r_>$ and a transverse coordinate represented by $r_<$. Convenient coordinates which describe the longitudinal and transverse modes throughout the (r_1, r_2) plane are the polar coordinates, $R = (r_1^2 + r_2^2)^{1/2}$ and $\alpha = \tan^{-1}(r_2/r_1)$, respectively. Thus, when one of the electrons escapes from the atom, R is large and therefore either $r_1 \gg r_2$ and $\alpha \sim 0$ or $r_2 \gg r_1$ and $\alpha \sim \pi/2$ identifies the valley in which the residual electron is trapped.

Ignoring the pd and higher partial waves, our wave function is the sum of two terms,

$$\psi = g_{sp}(r_1, r_2)Y_{011M}(\hat{r}_1, \hat{r}_2) + g_{ps}(r_1, r_2)Y_{101M}(\hat{r}_1, \hat{r}_2). \quad (21)$$

As a zeroth-order picture we can think of g_{sp} as satisfying a Schrödinger equation in r_1 and r_2 alone with the potential (20) averaged over all angles θ_{12} and with a centrifugal potential $0/r_1^2 + 1/r_2^2$. Similarly, we can think of g_{ps} as approximately satisfying its own equation. This view is of course not correct at small distances, where g_{sp} and g_{ps} are coupled, but it provides a plausible viewpoint for purposes

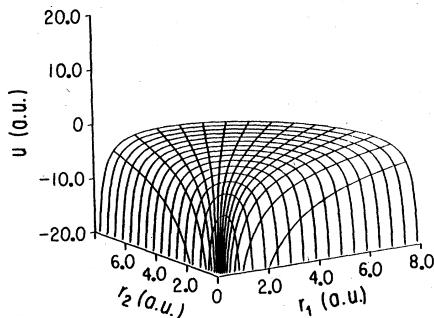


FIG. 2. Two-electron potential for helium given by Eq. (20) with $\theta_{12} = 180^\circ$.

of discussion. Upon including the centrifugal potentials for the s and p electrons, the effective potential clearly becomes asymmetric about $r_1 = r_2$ (i.e., about $\alpha = \pi/4$) in helium and also in all of the alkaline earths. Nonetheless, the *second* transverse eigenmode in the $l=0$ valley [i.e., the energy level of $\text{He}^+(2s)$, as opposed to the first eigenmode $\text{He}^+(1s)$] is very nearly degenerate with the *first* transverse eigenmode in the $l=1$ valley [i.e., $\text{He}^+(2p)$]. This, the so-called “accidental degeneracy,” becomes exact at large distances R in helium, allowing the wave function to retain an approximate $+/-$ symmetry (i.e., symmetry or antisymmetry about the line $r_1 = r_2$) even at infinity as it resonates between the two valleys. This resonance is no longer possible in the large- R limit for Be, since the $\text{Be}^+(2s)$ and $\text{Be}^+(2p)$ levels are not degenerate, but are split by $\Delta E \sim 0.3$ Ry. This nondegeneracy has little importance at small distances $R \lesssim 5$ a.u. since the local kinetic energy is then much larger than ΔE . Yet at larger distances it affects the wave function greatly, especially for low energies well below $\text{Be}^+(2s)$, as the kinetic energy available to the *longitudinal mode* becomes significantly different in the two valleys.

Figure 3 shows graphs of the $l_1=0, l_2=1$ component of the charge density, $[g_{sp}(r_1, r_2)]^2$, for the two eigenchannels $\alpha=1$ and 2 at three successive energies. (While we have been discussing g_{sp} and g_{ps} heuristically, as though they separately obeyed their own Schrödinger equation, our calculations include exactly their coupling by exchange.) Examining the $\alpha=1$ channel at the highest energy we see that the wave function is concentrated and approximately symmetric about $r_1 = r_2$ for r_1 and r_2 near the origin ($R \sim 0$). As the two-electron wave function propagates outward in R from the origin it meets a rising potential which is highest along the line $r_1 = r_2$, as seen in Fig. 2. In He the wave function breaks off this potential ridge, dividing into both valleys with comparable amplitudes.¹¹ The beryllium densities at a low energy, just above the $2s2p$ bound level, are shown in Fig. 3(a). This energy is so low that the “right-hand” valley, associated with $\text{Be}^+(2p)$ excitation, is strongly closed even at small distances $R \lesssim 4$ a.u. While the “left-hand” valley associated with $\text{Be}^+(2s)$ excitation is closed at $R \rightarrow \infty$, it is *locally open* at $R < R_0$ as evidenced by the negative curvature of g_{sp}^2 for $\alpha=1$ throughout the $2s$ valley ($r_1 \sim 0$). The orthogonal ($\alpha=2$) eigenchannel wave function is likewise forced into the $\text{Be}^+(2p)$ valley and its graph is dominated by the exponential increase of g_{sp} as r_1 increases. (Recall that boundary conditions at $r \rightarrow \infty$ are imposed at a later stage by MQDT procedures which superpose the $\alpha=1$ and 2 eigenchannel wave functions.) The vast difference between the longitudinal kinetic energies available in the two valleys effectively decouples these channels altogether, accounting for the nearly zero value of θ at this energy in Fig. 1(a). At this energy the wave-function components g_{sp} and g_{ps} are accordingly almost separable in independent-electron coordinates (r_1, r_2) .

A dramatic, qualitative change in the wave function ensues as the energy is increased. Figure 3(b) shows an intermediate energy, just above the $\text{Be}^+(2s)$ threshold, where the transition from no mixing to equal mixing has essentially been completed. The wave function now

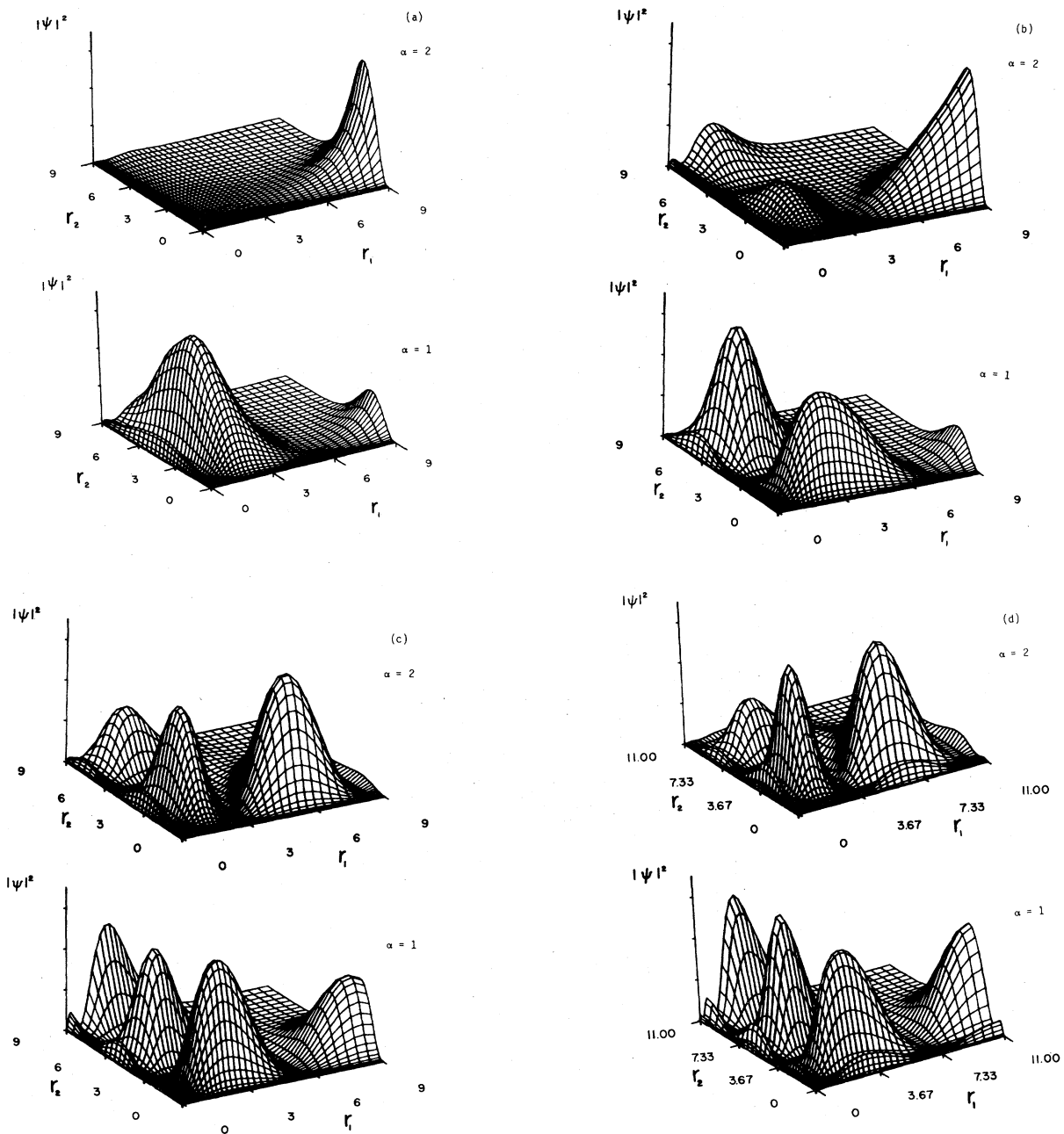


FIG. 3. The sp component of the charge density $|\Psi_\alpha|^2$ is shown as a function of the coordinates r_1 and r_2 at different excitation energies ϵ_1 . (a) The lower graph shows the $\alpha=1$ eigenchannel of beryllium while the upper graph shows the $\alpha=2$ eigenchannel at an energy $\epsilon_1 = -0.26$ Ry relative to the $2s$ threshold. (b) Same as (a), but at an energy $\epsilon_1 = 0.02$ Ry. (c) $\epsilon_1 = 0.26$ Ry. (d) The graph corresponding to (c) for magnesium, with $\epsilon_1 = 0.26$ Ry being the energy relative to the $3s$ threshold.

spreads with almost equal amplitude into each valley after encountering the potential ridge near $R \sim 4$. Exponential growth as r_1 increases in the $2p$ valley still overwhelms the $2p\epsilon s$ component of the wave function beyond $R \sim 6$, though not until it has accumulated the roughly π rad of de Broglie phase needed to establish the lowest autoionizing state, $2p3s$. Indeed, this energy lies within the decay width of that state.

Finally, Fig. 3(c) shows an energy close to the $2p$ thresh-

old, for which the local kinetic energy is now positive out to $r = r_0$ in each valley, although it is still negative along the line $r_1 = r_2$ beyond about $R = 4$ a.u. The $\alpha=1$ eigenchannel wave function shows a large lobe of density for $R < 4$ situated approximately symmetrically about $\alpha = \pi/4$, and this approximate symmetry holds all the way out to $r_0 \sim 9$, at least in the amplitude of the wave function. This state is the exact analog of the “+” state of Cooper, Fano, and Prats.³ Conversely, the orthogonal

TABLE II. Beryllium $1P^o$ quantum defects.

Level	Experiment (Ref. 13)	This calculation	Norcross and Seaton (Ref. 12)	I
2s 2p	0.166	0.085	0.151	0.110
2s 3p	0.296	0.235	0.283	0.181
2s 4p	0.332	0.319	0.322	0.202
2s threshold		0.389	0.374	

$\alpha=2$ eigenchannel wave function has a nodal line running generally close to the line $r_1=r_2$. At small R this nodal line diverts from the ridge and intersects the r_1 axis near 3 a.u., bearing a close resemblance to the behavior of the “-” state in helium shown in Fig. 1 of Ref. 2. Thus the difference between kinetic energies in the two valleys becomes insignificant at higher energies and the heliumlike “+/-” equipartition of the density between $2sep$ and $2pes$ is restored. This supports the view that the two-electron wave function encounters the ridge “suddenly” as R increases, which simply shears the wave function into two equal halves once the energy is sufficiently high.

In summary, we confirm the main points made by I: although the $2s$ and $2p$ levels are nondegenerate for Be, the nondegeneracy becomes unimportant at higher excitation energies in the critical region of configuration space ($R \sim 5$ a.u.) where the wave function breaks off of the potential ridge and into the valleys.

B. Beryllium energy levels and oscillator strengths

To determine the bound-state energy levels lying below the $\text{Be}^+(2s)$ threshold we must impose the boundary condition

$$\psi \rightarrow 0 \text{ as } r \rightarrow \infty \quad (22)$$

on the total wave function

$$\psi = \sum_{\alpha=1}^2 a_{\alpha} \psi_{\alpha}, \quad (23)$$

with ψ_{α} given by Eq. (17) in the region of configuration space exterior to the R -matrix volume V . The behavior of f and g as $r \rightarrow \infty$ is known analytically. They both have exponentially growing and decaying component at these negative energies. Equating to zero the coefficients of the exponentially rising part, so as to satisfy the boundary condition (22), we obtain a set of equations which determine the bound-state energy levels,⁶ i.e.,

$$\sum_{\alpha=1}^2 F_{i\alpha} a_{\alpha} = 0, \quad i=1,2 \quad (24)$$

$$F_{i\alpha}(\nu_1, \nu_2) = U_{i\alpha} \sin[\pi(\nu_i + \mu_{\alpha})], \quad (25a)$$

TABLE III. Oscillator strengths for Be.

Level	f_n (This calculation)	f_n (Ref. 14)
2s 2p	1.13	1.38
2s 3p	0.031	0.025
2s 4p	0.0019	0.0013

$$\epsilon_i = -\frac{1}{2\nu_i^2} = E - E_{\text{ion}}^i. \quad (25b)$$

Setting $\det\{F_{i\alpha}\} = 0$ we get an equation which relates ν_1 to ν_2 . A second relation between ν_1 and ν_2 is

$$E = E_{\text{ion}}^1 - \frac{1}{2\nu_1^2} = E_{\text{ion}}^2 - \frac{1}{2\nu_2^2}. \quad (26)$$

Solving for ν_1 we determine the bound-state energy levels shown in Table II in terms of quantum defects. The levels close to the $2s$ threshold show very good agreement with experiment. Norcross and Seaton,¹² by including such effects as the polarization of the $1s^2$ core, obtained more accurate values for the two lowest states.

The oscillator strength for the n th discrete level in terms of the MQDT parameters is⁶

$$f_n = \frac{2\omega(a_1 D_1 + a_2 D_2)^2}{N_n^2}, \quad (27)$$

where ω is the photon energy in a.u., μ is the quantum defect of the $2snp$ Rydberg levels, and

$$N_n^2 = \nu_{1n}^3 + \frac{\partial \mu}{\partial \epsilon}. \quad (28)$$

The dipole matrix elements for the eigenchannels (D_1, D_2) are given by Eq. (18) and a_1, a_2 are obtained from Eq. (24). A simple configuration mixing calculation including s^2 - and p^2 -type configurations was performed to obtain the ground-state wave function and energy (-1.016 a.u.). Table III gives our results for f_n , which agree with previous “state of the art” computations¹⁴ much better than the values obtained in I.

Figure 4 shows plots of D_1 and D_2 as functions of ener-

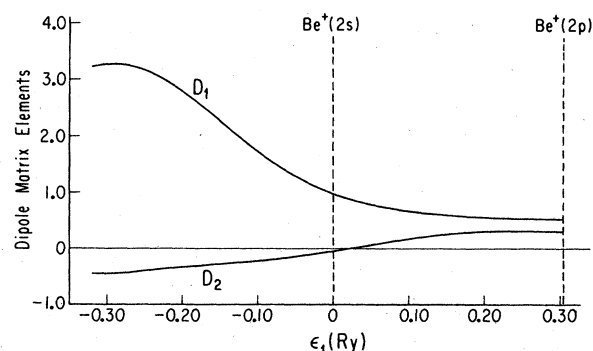


FIG. 4. The eigenchannel dipole matrix elements D_{α} ($\alpha=1,2$) are shown as functions of ϵ_1 , the energy relative to the $2s$ threshold of Be^+ .

gy. They reinforce the interpretation of the eigenchannel wave functions as being large (+) or small (-) near the origin ($R \sim 0$), as expected from the hyperspherical point of view.^{1,3} That is, D_1 is about six times bigger than D_2 due to its larger overlap with the ground state. The dipole amplitudes D_1 and D_2 normally are slowly varying functions of energy. However, in this case D_1 shows a large variation with energy due to the presence of a Cooper zero in the $s \rightarrow p$ transition just below threshold (see Sec. 4.5 of Fano and Cooper¹⁵).

C. Photoionization cross section

In calculating the photoionization cross section in the autoionization region we include the $2pnd$ channel and diagonalize the full 29×29 system. This energy region has two closed channels and one open channel. A brief summary of the MQDT formalism is given here but the reader is referred to Ref. 6 for the complete details.

Requiring the closed-channel components to decay exponentially as $r \rightarrow \infty$ and the open-channel wave functions to be of the form

$$\psi = \phi_{2s}(f_{\epsilon,p} \cos \delta - g_{\epsilon,p} \sin \delta), \quad r \geq r_0 \quad (29)$$

gives an equation analogous to Eq. (24),

$$\sum_{\alpha=1}^3 F_{i\alpha} a_{\alpha} = 0, \quad i = 1-3 \quad (30)$$

where

$$F_{i\alpha} = F_{i\alpha}(-\delta/\pi, \nu_2). \quad (31)$$

It thus yields Eq. (25a) with ν_1 replaced by $-\delta/\pi$. Setting $\det\{F_{i\alpha}\} = 0$ gives an equation for δ at any energy; the coefficients a_{α} are given for a particular energy by

$$a_{\alpha}^{(\delta)} = \frac{C_{i\alpha}}{\left[\sum_i C_{i\alpha}^2 \right]^{1/2}}, \quad (32)$$

where $C_{i\alpha}$ is the cofactor of the matrix element $F_{i\alpha}$. The cross section (in a.u.) then takes the form

$$\sigma = \frac{4\pi^2 \omega}{137} \frac{\left[\sum_{\alpha=1}^3 a_{\alpha}^{(\delta)} D_{\alpha} \right]^2}{N^2} \quad (33)$$

with the normalization factor

$$N = \sum_{\alpha} U_{i\alpha} \cos(-\delta + \pi \mu_{\alpha}) a_{\alpha}^{(\delta)}. \quad (34)$$

Here $i = 2s\epsilon p$ is the lone open channel in this energy range. Knowledge of $U_{i\alpha}$, μ_{α} , and D_{α} as functions of energy thus determines the cross section.

Figure 5 shows a plot of the photoionization cross section using the dipole velocity form (18) for the dipole matrix elements. The dipole length form gives a cross section with 20% higher peaks but with the same overall shape. The $2pnd$ series of resonances are very narrow, demonstrating the weak interaction between this channel and the other two. In contrast the $2pns$ resonances have very broad autoionization profiles showing a strong in-

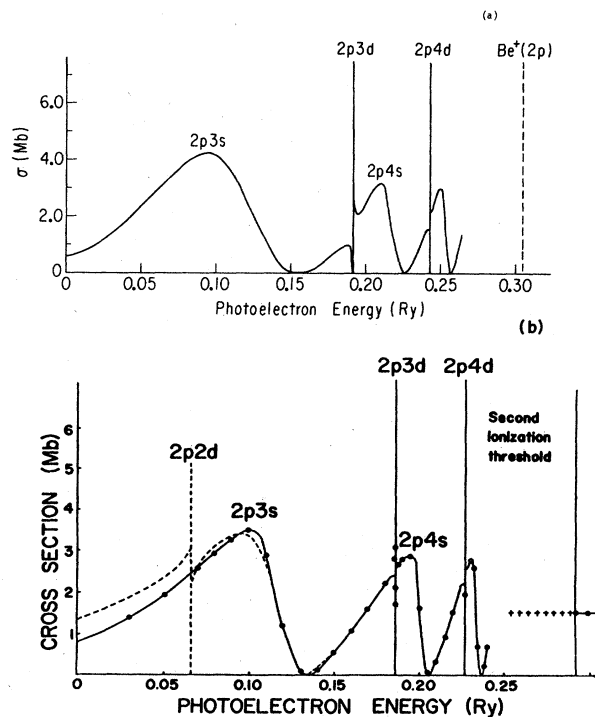


FIG. 5. The beryllium photoionization cross section is given as a function of the photoelectron energy using the dipole velocity form of the dipole matrix element: (a) this calculation, (b) Dubau and Wells (Ref. 17).

teraction with the background continuum as expected from our earlier discussion. In fact, these autoionizing states decay so rapidly that it does not make sense to consider them to be quasistable, even as a first approximation. We obtain good agreement with experiment¹⁶ and with previous calculations^{17,1} in this energy range.

D. Magnesium

We initially consider the two channels $3s\epsilon p$ and $3pns$ only, as we did for Be. Calculated mixing angles and eigenchannel quantum defects θ , μ_1 , and μ_2 are shown in Fig. 6. The mixing angle θ goes from 0 at low energies to approximately $\pi/4$ at high energies in the same way as in Be. Further verification of this equipartition rule is given in the plot of the sp component of the charge density for the K -matrix eigenchannel wave functions at $\epsilon = +0.26$ Ry in Fig. 3(d). Note the concentration in density about $r_1 = r_2$ where both electrons are near the nucleus (the + state) for $\alpha = 1$ and the approximate nodal line along $r_1 \simeq r_2$ for $\alpha = 2$ (- state). The similarity between Fig. 3(d) for magnesium and Fig. 3(c) for Be is striking. The analysis of the eigenmode breaking from the potential ridge and dividing with approximately equal amplitude into the $Mg^+(3s)$ and $Mg^+(3p)$ valleys follows in the same way as described in Sec. III A for Be.

We have also calculated some bound-state energies for Mg. In doing this we force the wave functions of the $3p\epsilon s$ channel to be zero on the boundary $r = r_0$, as joining to Coulomb functions for this strongly closed channel at low

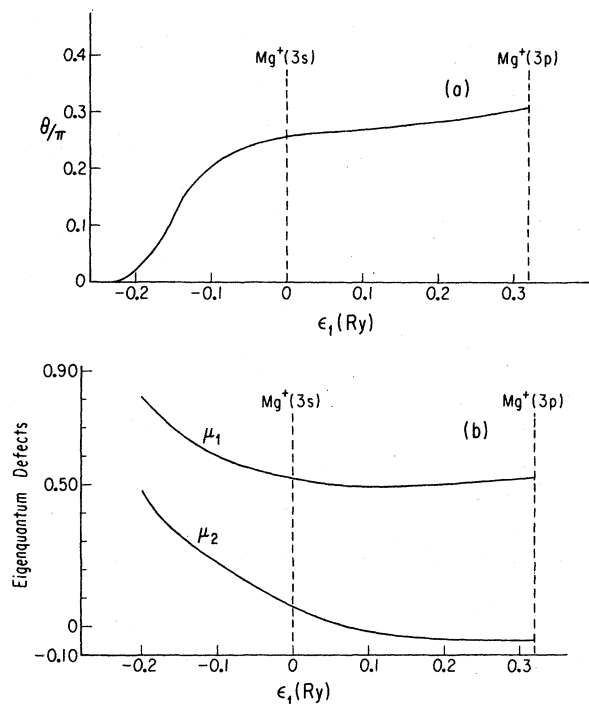


FIG. 6. Final-state quantum-defect parameters as functions of the energy relative to the $3s$ threshold: (a) mixing angle and (b) eigenquantum defects.

energies can lead to numerical difficulties. Table IV compares the experimental values¹³ with those calculated here and with a recent calculation¹⁸ which applied the Norcross-Seaton method to Mg. The agreement between the results is satisfactory considering our use of the crude Hartree-Slater model potential to represent the $e^- - Mg^{2+}$ interaction.

The photoionization cross section in the autoionizing region has been reported by several authors.^{19,16} A very recent study²⁰ attempted to measure the absolute cross section near the $Mg^+(3s)$ threshold. Our calculation proceeds as in Sec. III C. Figure 7 shows the photoionization cross section in the dipole velocity approximation. The dipole length calculation, as in Be, yielded 20% higher peaks but with the same general shape. Once again we see the narrow $3pnd$ resonances and the broad $3pns$ profiles corresponding to strong interaction with the $3sep$ channel. Stated more graphically, these $3pns$ autoionizing states decay before completing even half of a "Rydberg orbit." The first minimum above the $Mg^+(3s)$ threshold is the Cooper zero of the s to p transition, which had occurred below threshold in the discrete spectrum for Be. Our results show good agreement with previous photoionization calculations.²¹

TABLE IV. Magnesium quantum defects.

Level	Experiment (Ref. 13)	This calculation	Ref. 18
$3s\ 3p$	0.970	1.019	0.955
$3s\ 4p$	1.016	1.087	1.007

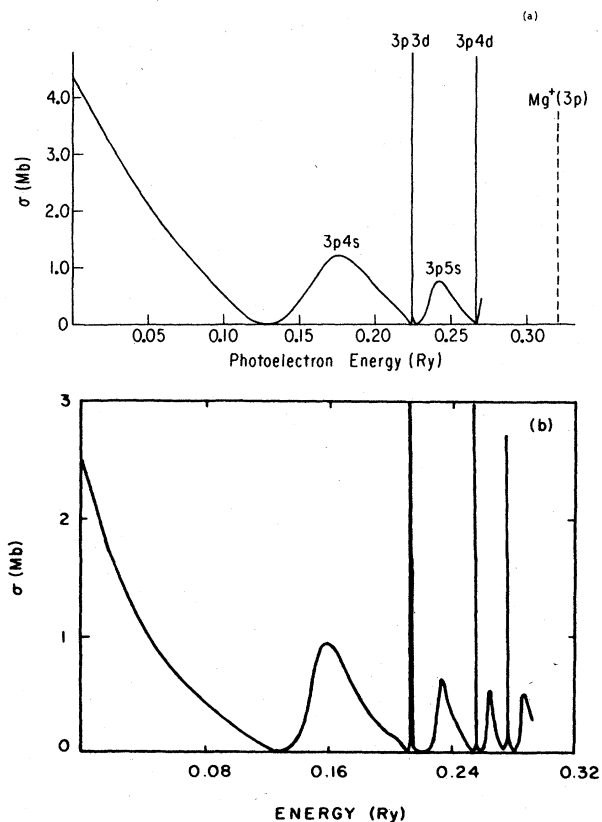


FIG. 7. Photoionization cross section for magnesium as a function of the photoelectron energy: (a) this calculation, (b) Bates and Altick (Ref. 21).

E. Ca, Sr, and Ba

The equipartition rule discussed in Sec. III was also seen in an empirical MQDT analysis⁴ of the $^1P^o$ discrete spectra of Ca, Sr, and Ba and reproduced by a coupled-channels calculation.²² One important difference between these elements and Be and Mg is that the first threshold above the ns threshold is the $(n-1)$ threshold, as opposed to the np threshold in Be and Mg. The two strongly interacting series are $nsn'p$ and $(n-1)dn'p$ for Ca ($n=4$), Sr ($n=5$), and Ba ($n=6$). One other difference is that the lowest levels of the $(n-1)dn'p$ series lie in the discrete spectrum of the $nsn'p$ series. Nevertheless, the angle θ characterizing the mixing between the two lowest channels is comparable for all the alkaline earths, as is shown in Table V. The values of θ/π for Be and Mg are taken

TABLE V. Mixing angles for the $^1P^o$ alkaline earths.

Atom	θ/π
^4Be	0.30
^{12}Mg	0.31
^{20}Ca	0.33
^{38}Sr	0.30
^{56}Ba	0.30
^{88}Ra	0.30

from this calculation at the lowest np threshold. The values for Ca, Sr, Ba, and Ra are taken from Ref. 4. While some analogous photoionization calculations^{22,23} have also been performed for Ca, Sr, and Ba, their explicit connection to Be and Mg has not yet been fully understood.

IV. DISCUSSION

In this work we have demonstrated that the noniterative formulation of the eigenchannel R -matrix method,⁵ using independent-electron basis functions, provides a simple and direct approach for studying the correlated motion of atomic electrons. The results required a relatively small-scale computational effort. We estimate that the entire final calculation at 14 different energies utilized approximately six minutes of central-processing-unit (CPU) time of a VAX 11/780 machine, which should translate into about 30 seconds on an IBM 3081. This time includes the calculation of energy-independent numerical basis functions in the Hartree-Slater potential, the calculation of all matrix elements including the dipole matrix elements, the solution of the linear eigenvalue problem at each energy, the matching to Coulomb functions, and the calculation of photoionization cross sections using quantum-defect theory. One difference of our approach from similar calculations is that we have used a basis of nonorthogonal continuum trial functions which are in turn not orthogonal to the target states, e.g., $2s$ and $2p$ of Be^+ . This provides an added flexibility which may prove quite useful in more complicated problems, although additional overlap integrals are then required in some of the matrix elements. One possible drawback, however, is that the addition of extra basis functions may result in a large redistribution in the values of the eigenvector components $c_k^{(\beta)}$, making it difficult to pin the correlations onto a limited number of basic functions with the largest eigenvector components. In this case the analysis of correlations may be confined to studying the eigenmodes Ψ_α in the r_1, r_2 space, as we have done in this paper, rather than examining the basis functions which contribute most to the makeup of that wave function.

In all R -matrix calculations the choice of the reaction volume is critical. Here this volume is the region of configuration space for which $\max\{r_1, r_2\} < r_0$. Clearly r_0 needs to be large enough to enclose all of the "correlated" regions in which the *probability of finding two electrons* (i.e., the exchange) is non-negligible. On the other hand, the convergence of the linear expansion (12) improves dramatically when r_0 is chosen as small as possible. Experimentation in the case of Be led to the choice $r_0 = 9$ a.u., though our results were identical with $r_0 = 11$ a.u. Magnesium, somewhat larger and softer, required $r_0 = 11$ a.u.

The choice of the R -matrix boundary r_0 is important for yet another reason. At sufficiently negative energies in any channel the eigenchannel wave functions diverge exponentially as r increases. When the channel energy is sufficiently negative this exponential growth dominates the variational calculation *within* the reaction volume, leading to numerical inaccuracies when these solutions are

matched to (exponentially large) Coulomb functions at $r = r_0$. That is, the calculation of Wronskians involves a subtraction of two large numbers, immediately giving a source of numerical error. When this situation arises we have found it important to *force* the strongly closed channel wave functions to vanish on the surface of the reaction volume by removing all trial functions nonzero at $r = r_0$ prior to solving the variational problem. Thus we impose the $r = \infty$ boundary condition at the beginning instead of at the end by the MQDT formulas. This procedure no longer permits extraction of channel mixing parameters such as θ , but the channel mixing is normally negligible in this situation anyhow.

This difficulty of strongly closed channels is most likely the origin of numerical errors in the calculation of I below the $2s$ level of Be^+ . (The discrepancy with our present results is greatest in the eigenquantum defects.) We suspect this for two reasons. First, the agreement between our present results and those of I is excellent above the $2s$ threshold. More fundamentally, I solved the coupled radial equations out to a matching radius $R_0 = 14$ a.u., which should have accentuated the numerical problems associated with exponential growth. This large choice of R_0 proved necessary in that work because of the slow convergence of the coupled equations in the hyperspherical radius R to the asymptotic of close-coupling form. (It has since been demonstrated elsewhere²⁴ that this difficulty can be largely circumvented by returning to independent-electron coordinates in the outer region, even if hyperspherical coordinates are used at small R .)

It is worth summarizing, nonetheless, the complementary nature of the earlier hyperspherical calculation¹ and the present R -matrix study. For the qualitative purposes of understanding the overall physical picture, the adiabatic hyperspherical method has distinct advantages. The potential curve plot of I permits a simple visualization of the critical regions in configuration space and in energy. On the other hand, for quantitative purposes of finding energy levels, oscillator strengths, and autoionization line shapes, the R -matrix method is unquestionably much easier to use. It is also easier to systematically improve on its accuracy, by changing the basis functions, r_0 , etc. The information about critical regions of configuration space and of energy is of course contained in the R -matrix variational wave functions, but it requires some effort to extract this information in the form of plots such as Fig. 3.

ACKNOWLEDGMENTS

One of us (P.F.O'M.) would like to thank Professor U. Fano for his continued guidance and support and Dr. K. T. Cheng for his assistance with the programming. The work performed at the University of Chicago was supported in part by the U.S. Department of Energy (Office of Basic Energy Sciences). The work performed at Louisiana State University was supported by the National Science Foundation and by an Alfred P. Sloan Foundation Fellowship.

- ¹(a) C. H. Greene, *Phys. Rev. A* **23**, 661 (1981); (b) for a recent review, see U. Fano, *Rep. Prog. Phys.* **46**, 97 (1983).
- ²J. W. Cooper, U. Fano, and F. Prats, *Phys. Rev. Lett.* **10**, 518 (1963).
- ³J. H. Macek, *J. Phys. B* **1**, 831 (1968).
- ⁴J. A. Armstrong, J. J. Wynne, and P. Esherick, *J. Opt. Soc. Am.* **69**, 211 (1979).
- ⁵C. H. Greene, *Phys. Rev. A* **28**, 2209 (1983); see also H. Le Rouzo and G. Raseev, *ibid.* **29**, 1214 (1984).
- ⁶K. T. Lu, *Phys. Rev. A* **4**, 579 (1971); C. M. Lee and K. T. Lu, *ibid.* **8**, 1241 (1973), and references therein. See also M. J. Seaton, *Rep. Prog. Phys.* **46**, 167 (1983).
- ⁷U. Fano and C. M. Lee, *Phys. Rev. Lett.* **31**, 1573 (1973).
- ⁸C. Laughlin and G. A. Victor, in *Atomic Physics 3*, Proceedings of the Third International Conference held at Colorado, 1972, edited by S. J. Smith and G. K. Walters (Plenum, New York, 1973).
- ⁹C. D. Lin, *J. Phys. B* **16**, 723 (1983).
- ¹⁰J. P. Desclaux, *Comput. Phys. Commun.* **1**, 216 (1969).
- ¹¹See Fig. 17 of Ref. 1(b).
- ¹²D. W. Norcross and M. J. Seaton, *J. Phys. B* **9**, 2983 (1976).
- ¹³C. E. Moore, *Atomic Energy Levels*, Natl. Bur. Stand. (U.S.) Circ. No. 467 (U.S. GPO, Washington, D.C., 1949), Vols. I–III.
- ¹⁴C. D. Lin and W. R. Johnson, *Phys. Rev. A* **15**, 1046 (1977).
- ¹⁵U. Fano and J. W. Cooper, *Rev. Mod. Phys.* **40**, 441 (1968).
- ¹⁶G. Mehlman-Balloffet and J. M. Esteve, *Astrophys. J.* **157**, 945 (1969).
- ¹⁷J. Dubau and J. Wells, *J. Phys. B* **6**, 1452 (1973).
- ¹⁸C. Mendoza, *J. Phys. B* **14**, 397 (1981).
- ¹⁹M. A. Baig and J. P. Connerade, *Proc. R. Soc. London, Ser. A* **364**, 353 (1978).
- ²⁰J. M. Preses, C. E. Burkhardt, W. P. Garver, and J. J. Leventhal, *Phys. Rev. A* **29**, 985 (1984).
- ²¹G. N. Bates and P. L. Altick, *J. Phys. B* **6**, 653 (1973); J. Dubau and J. Wells, *ibid.* **6**, L31 (1973).
- ²²K. C. Pandey, S. S. Jha, and J. A. Armstrong, *Phys. Rev. Lett.* **44**, 1583 (1980); J. A. Armstrong, S. S. Jha, and K. C. Pandey, *Phys. Rev. A* **23**, 2761 (1981).
- ²³P. Scott, A. E. Kingston, and A. Hibbert, *J. Phys. B* **16**, 3945 (1983).
- ²⁴B. L. Christensen-Dalsgaard, *Phys. Rev. A* **29**, 470 (1984), and private communication.